



## Phase transitions and equation of state of zirconium under high pressure

Simone Anzellini <sup>1</sup>, François Bottin,<sup>2,3</sup> Johann Bouchet,<sup>2,3</sup> and Agnès Dewaele <sup>2,3,\*</sup>

<sup>1</sup>*Diamond Light Source Ltd., Diamond House, Harwell Science and Innovation Campus, Didcot, Oxfordshire OX11 0DE, United Kingdom*

<sup>2</sup>*CEA DAM-DIF, F-91297, Arpajon, France*

<sup>3</sup>*Université Paris-Saclay, CEA, Laboratoire Matière en Conditions Extrêmes, 91680 Bruyères-le-Châtel, France*



(Received 20 March 2020; revised 15 October 2020; accepted 20 October 2020; published 10 November 2020)

X-ray diffraction measurements performed in a diamond anvil cell under quasihydrostatic conditions up to 142 GPa at 300 K evidence an  $\alpha$ -Zr  $\rightarrow$  (17 GPa)  $\omega$ -Zr  $\rightarrow$  (35 GPa)  $\beta$ -Zr phase transitions sequence. *Ab initio* molecular dynamics calculations performed on the body-centered cubic  $\beta$ -Zr at 300 and 1000 K and between 0 and 100 GPa produced an equation of state in excellent agreement with the experiments. The stability of  $\beta$ -Zr under pressure has been verified by numerical heating-quenching experiments, and the anharmonicity of the thermal vibrations has been evaluated. No dynamical instability due to a soft mode is evidenced between 25 and 100 GPa, in line with the experimental finding of a wide stability range for  $\beta$ -Zr.

DOI: [10.1103/PhysRevB.102.184105](https://doi.org/10.1103/PhysRevB.102.184105)

### I. INTRODUCTION

Zirconium is widely used for nuclear and chemical applications, owing to its low neutron absorption cross section and its resistance to corrosion. Its mechanical properties are similar to those of titanium, another group IVB metal of primary technological importance. Its chemical compounds, such as oxides and phosphates, are refractory and often used in applications for their resistance to thermal shock and their extremely low thermal conductivity. At ambient conditions, Zr crystallizes into a hexagonal close-packed (hcp) structure known as the  $\alpha$  phase. Under pressure ( $P$ ), it transforms to the  $\omega$  phase, similarly to Ti and Hf, a hexagonal structure which can be considered as a distortion of a body-centered cubic (bcc) phase [1,2]. By further compression at room temperature, Zr and Hf both adopt the  $\beta$  bcc phase, while Ti exhibits a more complex sequence of phase transitions, which is expected to conduct to the same bcc structure [3]. For all group IVB metals, the bcc phase can also be obtained by heating above room temperature at ambient pressure. For example,  $\beta$ -Zr is stable between 1136 and 2128 K, its melting point [1,4].

The  $\alpha \rightarrow \omega$  transitions (conditions, mechanism, kinetics) in group IV metals have been widely studied [3,5–8], as well as the temperature-induced  $\alpha \rightarrow \beta$  transitions, for which anharmonicity in lattice vibrations plays a leading role. Anharmonicity stabilizes  $\beta$ -Zr under high temperature [9]; under pressure, a lattice dynamics modeling evidenced three  $P$ - $T$  domains with different vibrational features for  $\beta$ -Zr [10]. At ambient temperature, Xia *et al.* [11] and Akahama *et al.* [12] measured Zr phases and equation of state in diamond anvil cells (DAC), using Au as the pressure transmitting medium (PTM) and marker, up to 32 and 68 GPa, respectively. Recently, Stavrou *et al.* [13] reported the experimental observation of an additional phase transition around 58 GPa at 300 K, from  $\beta$ -Zr to an isostructural phase called  $\beta'$ -Zr.

The observed phase transition was associated with a volume ( $V$ ) discontinuity of  $\approx 4\%$ . Stavrou *et al.*'s experiment was performed by compressing nonhydrostatically a Zr sample in a DAC and measuring the corresponding lattice parameters via x-ray diffraction (XRD). Experimental data were interpreted with density functional theory (DFT) simulations. The obtained 0 K compression curve did not evidence any phase transition. However, when a numerical sample was heated around 1000 K and successively quenched to 300 K, *ab initio* molecular dynamics (AIMD) predicted a discontinuity in the  $P$ - $V$  points of the final state, similar to the one observed experimentally. This was attributed to anharmonic lattice vibrations. The sole other reported example of an isostructural phase transformation in an element is the  $\alpha$ -Ce  $\rightarrow$   $\gamma$ -Ce [1] and this is supposed to be driven by electronic correlation effects [14]. Therefore, the  $\beta$ -Zr  $\rightarrow$   $\beta'$ -Zr transition, driven by anharmonicity, would be unique and have fundamental interest for condensed matter physics.

Very recently, Pigott *et al.* [15] performed several measurements of the room-temperature compression curve of Zr under both quasihydrostatic and nonhydrostatic conditions, finding no evidence of any phase transformation up to 70 GPa.

In the present study, we have studied the behavior of zirconium under high compression using both experimental and theoretical-numerical techniques. Experimentally, the  $\beta$ -Zr is observed up to 142 GPa, the highest pressure reached. The measured and predicted equations of state are almost identical and close to the compression behavior of titanium [3]. Our results are presented below and discussed in the perspective of the available literature.

### II. METHODS

#### A. Experiments

Four runs have been carried out. For each run, one or several grains of Zr (approximately 5  $\mu$ m each; Alpha Aesar powder grain, 99.2 wt.% purity for runs 1 and 2, 98.8 wt.%

\*agnes.dewaele@cea.fr

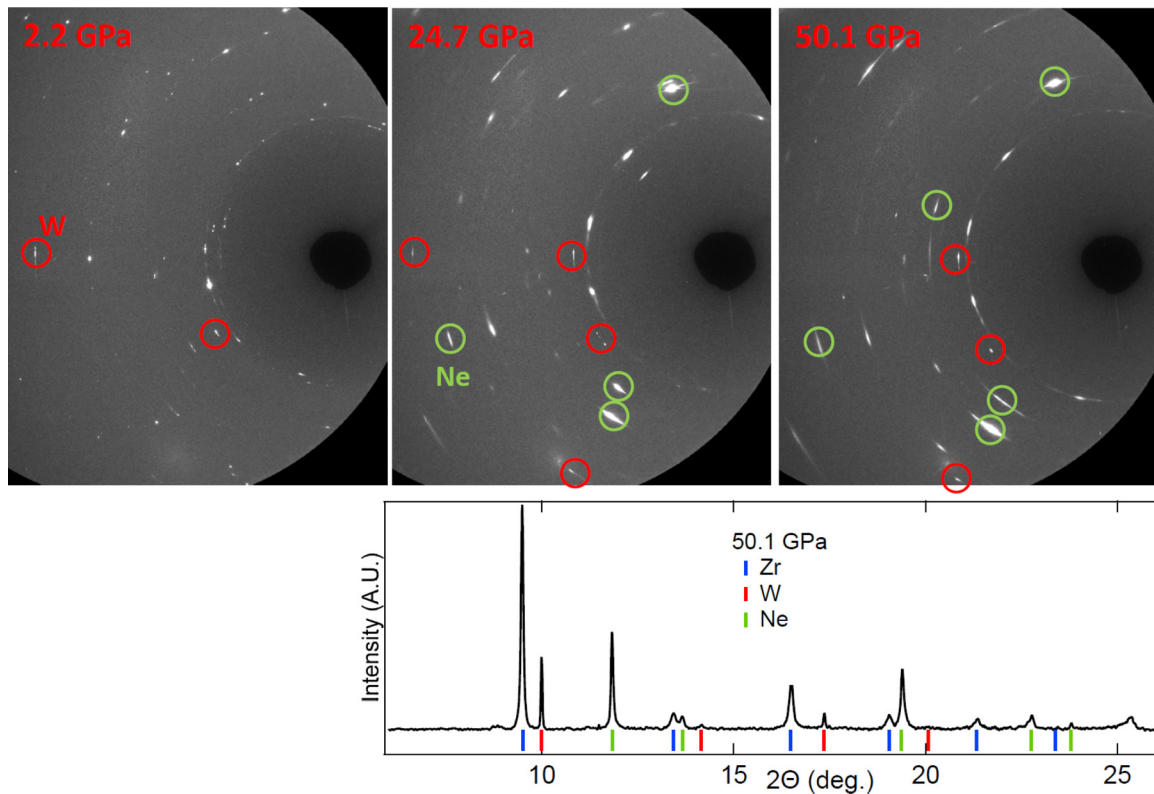


FIG. 1. Top panel: Selected XRD images collected in run 2. The XRD signal arises from Ne (circled in green), W (circled in red), and Zr (remaining signal). At 2.2, 24.7, and 50.1 GPa, Zr is under the  $\alpha$ ,  $\omega$ , and  $\epsilon$  phases, respectively. Bottom panel: Integrated pattern corresponding to the right image on the top panel. The ticks correspond to the predicted diffraction angles for  $\beta$ -Zr (body-centered cubic with lattice parameter  $a = 3.195 \text{ \AA}$ ), W (body-centered cubic with lattice parameter  $a = 3.035 \text{ \AA}$ ), and Ne (face-centered cubic with lattice parameter  $a = 3.142 \text{ \AA}$ ).

purity for runs 3 and 4) was loaded into each chamber. Different pressure standards (Ruby sphere in run 1, W in runs 2–4) were also added a few  $\mu\text{m}$  from the Zr sample. Finally, the He or Ne pressure-transmitting medium was loaded into the cell.

Diffraction data for runs 1 and 2 were collected at beamline ID27 (European Synchrotron Radiation Facility, Grenoble, France) [16] using a monochromatic x-ray beam ( $\lambda = 0.3738 \text{ \AA}$ ) focused down to  $2 \times 3 \mu\text{m}$  and measured using a MAR-CCD detector for runs 1 and 2. Runs 3 and 4 have been carried out at beamline I15 of Diamond Light Source [17], using a monochromatic beam ( $\lambda = 0.4246 \text{ \AA}$ ), a  $20 \times 20 \mu\text{m}$  spot size on the sample, and a MAR345 image plate detector.

In all runs, the detector geometry was calibrated with a  $\text{LaB}_6$  standard using the powder calibration routines of the DIOPTAS software suite [18]. Masks were applied to the raw diffraction images on a per-image basis before they were azimuthally integrated using the processing tools in the DIOPTAS suite. Diffraction data were analyzed by Le Bail fitting using the routines of the TOPAS software suite [19], and literature values for the lattice parameters of each phase were used as a starting point for these refinements.

During the experiment, pressures inside the high-pressure chamber of the DACs were measured using the ruby luminescence method (calibration from Ref. [20]) or the unit cell volume of W (calibration from Ref. [21]).

During the experiment, the sample was compressed up to 25 GPa in run 1 (under He), 62 GPa in run 2 (under Ne), 45 GPa in run 3 (under He), and 142 GPa in run 4 (under

He). Run 3 was interrupted early, due to a leak of the helium pressure medium through a fracture in the gasket at 45 GPa. This resulted in a direct compression of the sample between the two diamonds and a pressure decrease down to 33 GPa. Two additional data points were collected under these conditions before the pressure was completely released and the run ended. The measurements done in the first run have been already published elsewhere [7].

Figure 1 shows the evolution of the XRD patterns collected in run 2 as the pressure increases. All the XRD spots correspond to Zr, W, or Ne (above 5 GPa). At low pressure, the  $\alpha$ -Zr sample contains several single-crystal grains. Their number decreases at the  $\alpha$ -Zr  $\rightarrow$   $\omega$ -Zr transformation, as noted in Ref. [7] and as analyzed in Ref. [8]. The  $\omega$ -Zr  $\rightarrow$   $\beta$ -Zr only mildly affects the microstructure, with a similar number of XRD spots and an orientation of  $\beta$ -Zr grains clearly inherited from the orientation of  $\omega$ -Zr grains.

## B. Density functional theory simulations

*Ab initio* calculations have been performed using the electronic structure code ABINIT [22]. A projector augmented wave [23,24] (PAW) atomic data has been generated for zirconium using the ATOMPAW code [25] in the XML (Extensible Markup Language) format [26], considering 12 electrons in the valence and a cutoff radius of 2.2 bohr, leading to a cutoff energy equal to 400 eV. Exchange and correlation energy has been treated within the generalized gradient approximation

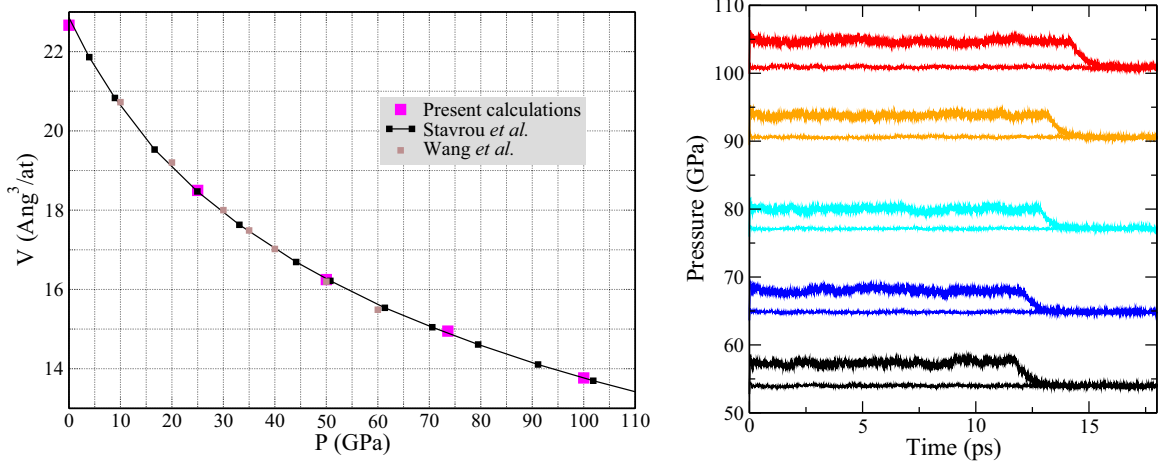


FIG. 2. Left panel: 0 K equation of state of  $\beta$ -Zr obtained by present *ab initio* calculations (magenta solid squares), by Stavrou *et al.* [13] (black solid line and points), and by Wang *et al.* [28] (brown solid squares). Right panel: AIMD trajectories at 300 K (thin solid lines) and 1000 K and then quenched at 300 K (thick solid lines) at several compressions between 50 and 100 GPa.

(GGA) using the Perdew-Burke-Ernzerhof (PBE) functional [27]. Using these computational details, we obtained an athermal compression curve of  $\beta$ -Zr in very good agreement with literature studies based on a GGA description of the electronic interactions [13,28] (see left panel of Fig. 2).

In order to reproduce the isostructural transition described by Stavrou *et al.* [13], we tried to mimic their molecular dynamics calculations. We performed AIMD simulations for several pressures between 0 and 100 GPa (around 0, 25, 50, 65, 75, 90, and 100 GPa) and two kinds of thermalization: the first one at 300 K and the second one at 1000 K, followed by a quench at 300 K. The supercell included 128 atoms, put in their high-symmetry bcc positions as starting point of the simulations. A careful treatment of the electronic density integration has been carried out with the use of a  $(2 \times 2 \times 2)$  **k**-point Monkhorst-Pack (MP) mesh [29]. As this leads to a strong increase of the overall time of calculation, an efficient scheme of parallelization was employed in order to reduce the human restitution time with hundreds to thousands of processors involved in each run [30]. We used a time step equal to 1.5 fs for the integration of the motion equations and equilibrated the system in the NVT canonical ensemble (constant number of particles, constant volume, and temperature) during thousands of time steps, which leads to at least 10-ps-long trajectories for each pressure at 300 or 1000 K, or after the quench (see right panel of Fig. 2).

### III. EXPERIMENTAL DATA ANALYSIS

#### A. Stress state

A standard analysis was performed in order to evaluate the pressurizing conditions of the sample in run 4, which reached the highest pressure. Under nonhydrostatic compression, the XRD peaks measured in a conventional DAC geometry are shifted from those measured under hydrostatic compression by an amount which depends on the peak class [31,32]. The gamma plots in Fig. 3 represent the lattice parameter corresponding to each XRD line [ $a_{hkl} = d_{hkl} \times \sqrt{(h^2 + k^2 + l^2)}$ ], as a function of diffraction angle  $2\theta$  and  $\Gamma_{hkl}$ . In short, it shows

the deviation of the XRD lines from the cubic symmetry, due to nonhydrostatic (deviatoric) stress. The model and notations are presented in Ref. [32]. Under nonhydrostatic compression, this plot shows a linear trend with a slope proportional to the deviatoric stress. In this case, a deviatoric stress of less than  $\approx 2$  GPa is obtained using the present gamma plots and the elastic parameters reported in Ref. [33].

A broadening in the FWHM (full width at half maximum) of the XRD lines is a sign of an increase in the microstress  $\sigma$ , which can be evaluated from the XRD signal following the equation used in Refs. [32,34]:

$$(\text{FWHM} \cos \theta)^2 = (2\sigma)^2 \frac{\sin^2 \theta}{E_{hkl}^2} + [\text{FWHM}(\sigma = 0) \cos \theta]^2, \quad (1)$$

where  $\theta$  is the diffraction angle and  $E_{hkl}$  is the single-crystal Young modulus of Zr [32,33]. Figure 4 represents  $(\text{FWHM} \cos \theta)^2$  versus  $\sin^2 \theta / E_{hkl}^2$  at three pressures. Although the general values of the measured FWHM are quite high, their pressure-induced variation is only mild: There is no clear evidence of any pressure-induced microstress on the Zr sample.

#### B. Equation of state of $\alpha$ -Zr, $\omega$ -Zr, $\beta$ -Zr

The  $P$ - $V$  data obtained in the present experiment are plotted in Fig. 5, together with the ones from Xia *et al.* [11], Akahama *et al.* [12], Stavrou *et al.* [13], and Pigott *et al.* (quasihydrostatic compression data) [15]. The volume measured by Stavrou *et al.* is lower than the present one, in the  $\omega$ -Zr and  $\beta$ -Zr phases, by up to 6%. Among the two  $P$ - $V$  data sets collected by Pigott *et al.* under quasihydrostatic compression, one agrees perfectly with ours, while the other differs by 3%.

The current  $P$ - $V$  data points have been fitted with a Rydberg-Vinet [35] equation of state formulation for each phase. The fitted parameters are listed in Table I and compared with the same parameters for Ti [3]. Subscript 0 indicates the reference state, ambient pressure. Ti and Zr EoS parameters  $K_0$  (bulk modulus) and  $K'_0$  (its pressure derivative) are close in each of the considered phases. The current data points for

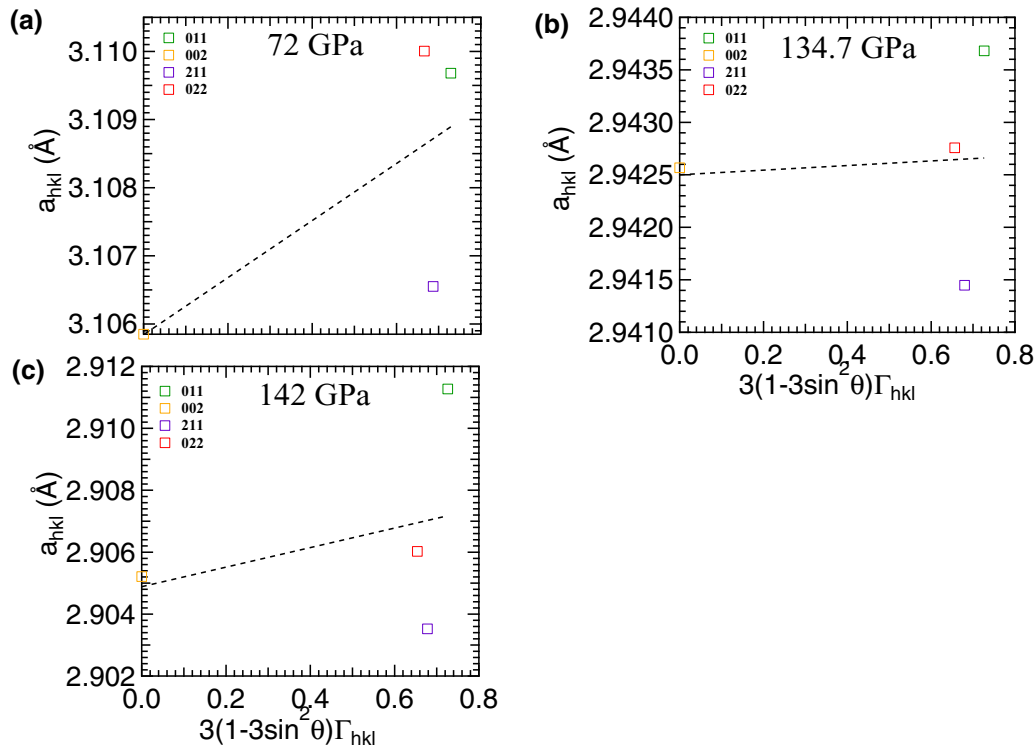


FIG. 3. Gamma plots for  $\beta$ -Zr, evaluated at selected pressures in run 4, on the basis of the diffraction angles  $2\theta$  for four x-ray diffraction lines (Miller indexes in the legend).

$\beta$ -Zr agree with the DFT-GGA results at 0 K, as in the case of titanium [3].

We have also fitted the experimental points of Stavrou *et al.* [13] with a Rydberg-Vinet equation of state [35] for each phase ( $\omega$ -Zr,  $\beta$ -Zr,  $\beta'$ -Zr).  $\omega$ -Zr and  $\beta$ -Zr are more compressible in Stavrou *et al.*'s work than in this study.

The difference between the experimental  $P$ - $V$  points measured in the current study and the ones reported in Stavrou *et al.* is striking and cannot be explained by the  $\approx 0.1\%$  uncertainty in the volume measured by XRD. Pressure metrology could be at play: Stavrou *et al.* use an Au x-ray pressure gauge, but the equation of state used for its calibration is not provided.

Here, the Zr sample is compressed in a soft PTM (Ne or He), while Stavrou *et al.* use no medium. In this case, the nonhydrostatic stress is limited by the yielding of the sample

itself, and a radial pressure gradient builds. It can reach several GPa/ $\mu\text{m}$  [36,37], which can affect the EoS measurement if the sample is not located close enough to the pressure gauge. Figure S1 in Stavrou *et al.* suggests that the Au x-ray marker was located several microns away from the sample analyzed with XRD, as no signal of Au is seen in these diffractograms. A pressure difference between sample and pressure marker is thus possible. In addition, the XRD peaks measured in a conventional DAC geometry under nonhydrostatic compression are shifted from those measured under hydrostatic compression [31,32], which also biases the equation of state. Reference [38] provides several examples of controversies on phases or equations of state which were later attributed to a nonhydrostatic compression bias. We suggest that this effect can also explain the difference between the current and the Stavrou *et al.* EoS measurements.

TABLE I. Rydberg-Vinet equation of state parameters obtained in this study and in the literature [3,13] using the same technique. The bold numbers have been fixed during the fit. The error bars on the last digit(s) correspond to the 95% confidence interval. The parameters listed for the  $\beta$ -Ti are an output from a fit of the high-temperature  $P$ - $V$  data and have higher error bars than the others.

Zirconium				Titanium			
Phase	$V_0$ ( $\text{\AA}^3/\text{at}$ )	$K_0$ (GPa)	$K'_0$	Phase	$V_0$ ( $\text{\AA}^3/\text{at}$ )	$K_0$ (GPa)	$K'_0$
$\alpha$ -Zr (this study)	23.29(1)	99.3(1.2)	2.92(13)	$\alpha$ -Ti [3]	17.65(2)	110.4(2.7)	<b>4</b>
$\omega$ -Zr (this study)	23.27(11)	78(7)	4.45(62)	$\omega$ -Ti [3]	17.46(10)	106.9(6)	3.68(20)
$\beta$ -Zr (this study)	<b>22.6</b>	93(1)	3.20(9)	$\beta$ -Ti [3]	17.8	96	3.1
$\omega$ -Zr [13]	<b>23.6</b>	78(6)	2.95(70)				
$\beta$ -Zr [13]	<b>22.6</b>	80(5)	3.35(40)				
$\beta'$ -Zr [13]	22.5(6)	43(5)	<b>6</b>				



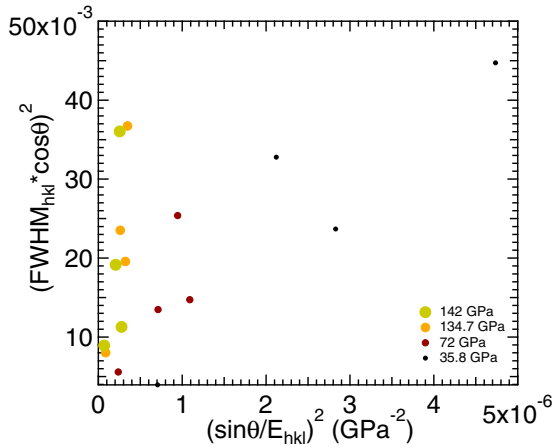


FIG. 4. Functions of FWHM (full width at half maximum), diffraction angle  $\theta$  (in deg), and single-crystal Young modulus of Zr  $E_{hkl}$  [33], which allow evaluating the microstress. The microstress is proportional to the slope formed by all points recorded at the same pressure [32].

It is interesting to note that the two data points collected in run 3 (empty red squares in Fig. 5) after the PTM escaped from the high-pressure cavity (therefore with the sample directly compressed between the diamond anvils) get closer to Ref. [13]’s measurements. This strengthens the hypothesis that the measured Zr equation of state is affected by the stress state of the sample.

In average, the measurements of  $\beta$ -Zr EoS up to 64 GPa by Akahama *et al.* [12] under nonhydrostatic conditions agree with ours; in these experiments, Zr and pressure marker XRD signals were collected on the same point, which prevents errors due to pressure gradients. An  $\approx 1\%$  decrease in measured volume at 56 GPa was interpreted as a possible evidence for a phase transition in  $\beta$ -Zr [12]. A close look at Fig. 5 suggests that this apparent decrease is within Akahama *et al.*’s  $P$ - $V$  data scatter, which is also of the order of 1%.

The  $P$ - $V$  points measured by Pigott *et al.* [15] are different (by up to 3%) in the two experimental runs they have conducted, with the same XRD technique, sample composition, and x-ray pressure marker (platinum). The sample pictures show that in one run, sample and marker were clearly embedded in pressure-transmitting medium, but not in the second run (which data deviate from ours), where metallic foils fill most of the high-pressure cavity. A direct nonhydrostatic compression between the diamond anvils affects the apparent EoS [31,32]. We propose this explanation for the lack of consistency between the measurements reported by Pigott *et al.*

### C. Stability domain of $\beta$ -Zr

In the present experiment, the  $\alpha \rightarrow \omega$  transformation was observed around 14–20 GPa with a 1.5% volume decrease and the  $\omega \rightarrow \beta$  transformation was around 35 GPa with a 2% volume decrease. The compression curves measured in runs 2 and 4 show no discontinuity between 35 and 142 GPa. This is a different observation from Stavrou *et al.* [13], who report an isostructural  $\beta$ -Zr  $\rightarrow \beta'$ -Zr with a 4% volume collapse at 58 GPa, larger than the  $\approx 1\%$  decrease observed by Akahama *et al.* [12]. In Zr, the  $\alpha \rightarrow \omega$  transition pressure

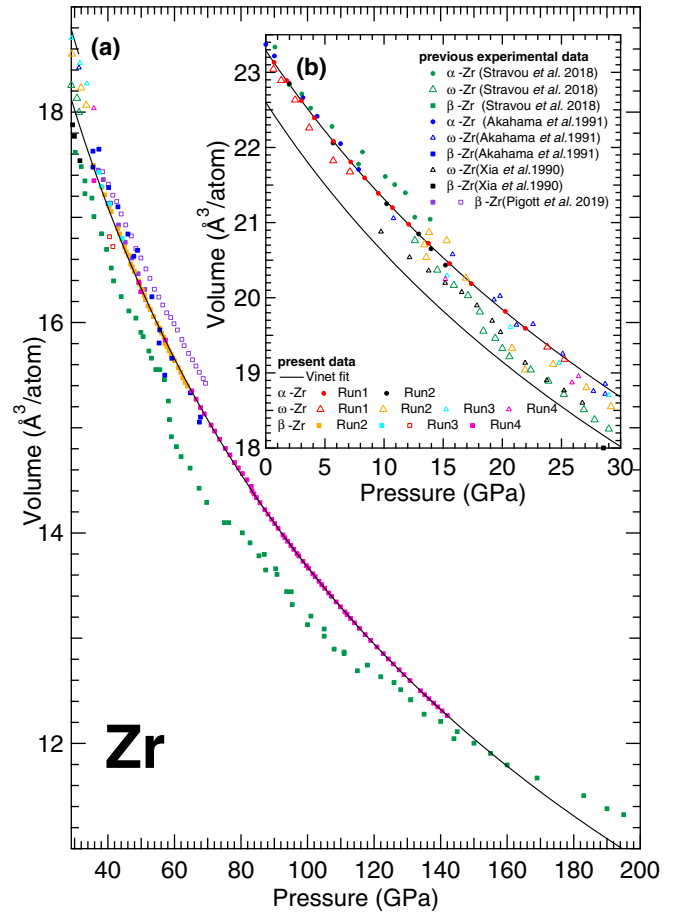


FIG. 5.  $P$ - $V$  data points for the three phases of Zr collected at 300 K in this study and Refs. [7,12,13,15]. (a)  $P$ - $V$  points collected for  $\beta$ -Zr and (b)  $P$ - $V$  points collected for  $\alpha$ -Zr and  $\omega$ -Zr. The two empty red squares are data collected in run 3 during a direct compression of the sample between the diamond anvils. Black solid lines correspond to fits of  $\alpha$  and  $\beta$ -Zr  $P$ - $V$  points obtained in the present study.

is sensitive to the chemical composition of the sample [39]. There is evidence that impurities impede the grain growth of  $\omega$  phase; an overshoot of 5.2 GPa is then necessary to induce the transition if the impurity level is increased by  $\approx 2$  wt.%, from ultrapure to a commercially available sample [40]. The samples used here and in Ref. [13] are all commercial; their impurity level varies by 0.7 wt.%. It is not expected that impurities affect drastically the equation of state; on the other hand, nonhydrostatic stress affects it [31,32], and the equations of state measured here and in Stavrou *et al.* are different. We thus suggest that the different stability observed for  $\beta$ -Zr is related to nonhydrostatic stress effects rather than impurities. The apparent isostructural  $\beta$ -Zr  $\rightarrow \beta'$ -Zr transition could be caused by a change in stress distribution in the course of the compression, for instance, due to the deformation (“cupping”) of the diamond anvils [41].

### IV. AB INITIO MOLECULAR DYNAMICS SIMULATIONS

Here, we followed the methodology proposed by Stavrou *et al.* [13]: The system is heated up to 1000 K, equilibrated

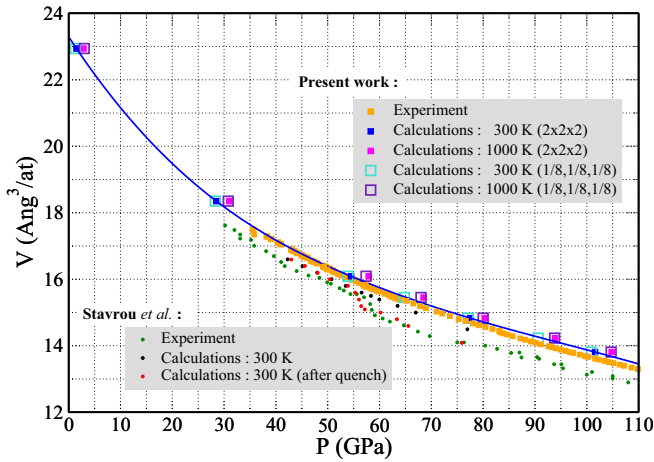


FIG. 6.  $\beta$ -Zr equation of state by means of AIMD simulations at two temperatures (300 and 1000 K) between 0 and 100 GPa, for two  $\mathbf{k}$ -point meshes: a  $(2 \times 2 \times 2)$  MP mesh and the single  $(\frac{1}{8}, \frac{1}{8}, \frac{1}{8})$   $\mathbf{k}$ -point. The plotted points are listed in Table II and comparisons are made with the present experimental data and the results obtained by Stavrou *et al.* [13]. The blue solid line corresponds to a fit of the 300 K present calculations.

during 10 ps, then cooled down at 300 K, and equilibrated again. The 300 K  $P$ - $V$  points reproduce perfectly the EoS obtained in the present experiments. As shown in Fig. 6 and Table II, we were not able to evidence the isostructural phase transition reported by Stavrou *et al.* (a 5-GPa reduction of the pressure at constant volume).

Surprised by this disagreement, we examined the calculation details on both sides. The most significant difference is that Stavrou *et al.* did not perform AIMD simulations using a  $(2 \times 2 \times 2)$  MP mesh but using one  $(\frac{1}{8}, \frac{1}{8}, \frac{1}{8})$   $\mathbf{k}$  point. Other parameters could affect the results, but to a lesser extent: the cooling rate (100 K/ps versus 500 K/ps in the present work), the number of atoms in the supercell (125 atoms versus 128 atoms in the present work), and the pseudopotential (norm-conserving versus PAW in the present work). We thus performed the simulations using the single  $(\frac{1}{8}, \frac{1}{8}, \frac{1}{8})$   $\mathbf{k}$  point. The  $V(P)$  points are close to those obtained with a converged MP  $\mathbf{k}$ -point mesh, although distinguishable (see Fig. 6 and Table II). We still did not observe any phase transition.

TABLE II. Pressure (in GPa) as a function of the volume (in  $\text{\AA}^3/\text{atom}$ ) obtained after AIMD calculations for two temperatures and two  $\mathbf{k}$ -point meshes: a  $(2 \times 2 \times 2)$  MP mesh and a single  $(\frac{1}{8}, \frac{1}{8}, \frac{1}{8})$   $\mathbf{k}$  point.

Volume	$(2 \times 2 \times 2)$ MP mesh			$(\frac{1}{8}, \frac{1}{8}, \frac{1}{8})$ $\mathbf{k}$ point		
	300 K	1000 K	Quench	300 K	1000 K	Quench
22.94	1.5	2.9		1.3	3.0	1.3
18.35	28.5	31.0		28.3	30.8	28.4
16.09	54.5	57.9	54.5	53.9	57.4	53.9
15.45		68.5	65.3	64.8	68.0	64.8
14.83	77.5	80.3	77.6	77.1	80.0	77.1
14.23		93.9	91.3	90.6	93.8	90.6
13.81	101.6	104.8	101.6	100.9	104.7	100.8

Stavrou *et al.* claim that anharmonicity induces this isostructural transformation. They equilibrated the system in a high-temperature state (1000 K) during a long time (10 ps) in order to capture the effects coming from the anharmonic part of the potential before cooling it down at 300 K and carrying out the transition. In the present calculations, we were not able to reproduce this behavior. In order to understand the impact of anharmonicity on this system, we have applied a method able to account for intrinsic effects of temperature on lattice dynamic properties.

## V. ANHARMONICITY IN $\beta$ -Zr

### A. Temperature-dependent effective potential

A few years ago, Hellman *et al.* [9,42,43] proposed a method called temperature-dependent effective potential (TDEP) to capture the anharmonic effects in solids in an effective way. Let us consider that the potential energy can be expanded around equilibrium positions as a function of interatomic force constants (IFC)  $\Phi_{i_1 \dots i_p}^{(p) \alpha_1 \dots \alpha_p}$  and displacements  $u_{i_k}^{\alpha_k}$  such as

$$U = U_0 + \sum_{p \geq 1} \frac{1}{p!} \sum_{\substack{\alpha_1 \dots \alpha_p \\ i_1 \dots i_p}} \Phi_{i_1 \dots i_p}^{(p) \alpha_1 \dots \alpha_p} \prod_{k=1}^p u_{i_k}^{\alpha_k} \quad (2)$$

with  $U_0$  being the minimum of the potential energy. In this equation, the Latin letters in subscripts  $i, j, k, \dots$  and the Greek letters in superscripts  $\alpha, \beta, \gamma, \dots$  define the atoms and the Cartesian directions, respectively. By using the forces and displacements coming from the AIMD simulations, it is then possible to perform a fit of the IFC using a least square method. In this case, we no longer obtain the real IFC but effective ones  $\Theta_{i_1 \dots i_p}^{(p) \alpha_1 \dots \alpha_p}$  depending on temperature. If the expansion performed in Eq. (2) is cut at the second order, the AIMD energy writes at each time step  $t$

$$U_{MD}(t) = U_0 + \frac{1}{2} \sum_{\alpha\beta, ij} \Theta_{ij}^{\alpha\beta} u_{MD,i}^{\alpha}(t) u_{MD,j}^{\beta}(t). \quad (3)$$

Using these effective IFC, one can compute the phonon frequencies with their temperature dependency coming from the anharmonicity. We have implemented this method in the ABINIT package [44] (A-TDEP) and applied it with success to several systems [45,46]. In particular, we have shown that this approach is able to account for the stabilization of the uranium and plutonium bcc phase around 1000 K [47,48], highlighting the strong anharmonic effects present in these materials at high temperature.

### B. Phonon spectra as a function of temperature and pressure

At 0 GPa and room temperature, the bcc structure of zirconium is known to be unstable. Under these conditions, all the 0 K calculations performed at the harmonic level using finite differences method or density functional perturbation theory (DFPT) show soft modes in the phonon spectrum around  $\omega$  (corresponding to  $\mathbf{q} = (2/3, 2/3, 2/3)$  along the H-P high-symmetry line) and  $\Gamma$  point (see Refs. [28,49] and present

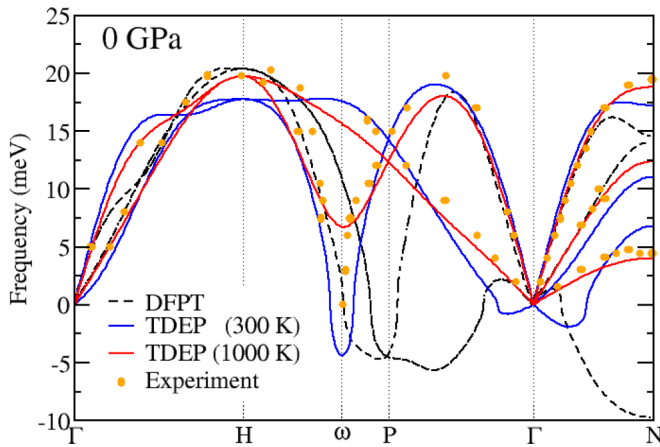


FIG. 7. Phonon spectra of  $\beta$ -Zr at 0 GPa calculated using (i) the DFPT implementation of ABINIT (black dashed line) and (ii) A-TDEP for two temperatures: 300 K (blue solid line) and 1000 K (red solid line). Experimental data (orange solid points) have been collected at 915°C [50].

DFPT calculations in Fig. 7). As demonstrated in the seminal work of Hellman *et al.* [9] and reproduced by our homemade implementation [44], the soft modes calculated at 0 K are also disclosed by A-TDEP at 300 K (see the blue solid line in Fig. 7) but are suppressed when the temperature increases, in agreement with the experimental observation establishing that  $\beta$ -Zr is stable above 1135 K. Around 1000 K, the calculated

and measured [50] phonon spectra agree very well (see the red solid line in Fig. 7).

In Fig. 8, we show the phonon spectra obtained with A-TDEP at 300 and 1000 K for pressures of 25, 50, 75, and 100 GPa. When AIMD simulations are performed using a  $(2 \times 2 \times 2)$  MP mesh, there are no soft modes: All the branches of the phonon spectra (solid lines in Fig. 8) are positive, whatever the temperature. This behavior unveils the dynamical stabilization of the bcc phase at high pressure, in line with experiments. At high pressure, the anharmonic effects disclosed by the difference between the 300 and 1000 K phonon spectra appear to be very low compared to the ones observed at 0 GPa.

Conversely, when AIMD simulations are performed using a single  $(\frac{1}{8}, \frac{1}{8}, \frac{1}{8})$   $\mathbf{k}$  point as in Stavrou *et al.* calculations, the phonon spectra (dashed lines in Fig. 8) differ from the ones obtained with the converged mesh. Soft modes similar to the ones calculated at room pressure and 300 K are observed around the  $\Gamma$  point along the [011] direction, suggesting that the structure is still unstable up to 75 GPa, in contradiction with experiments.

From these observations, we infer that an unphysical instability affects AIMD of the system when a single  $(\frac{1}{8}, \frac{1}{8}, \frac{1}{8})$   $\mathbf{k}$  point is used. An equilibration at high temperature (1000 K), with a soft mode in the AIMD, could push the system to another “bcc-like” structure, which would freeze at 300 K. As shown in Fig. 9, the  $\beta$  phase of zirconium is never dynamically stable at 300 K when the  $(\frac{1}{8}, \frac{1}{8}, \frac{1}{8})$   $\mathbf{k}$  point is used ( $C' < 0$  on the whole range of pressure [0 GPa; 100 GPa]) and

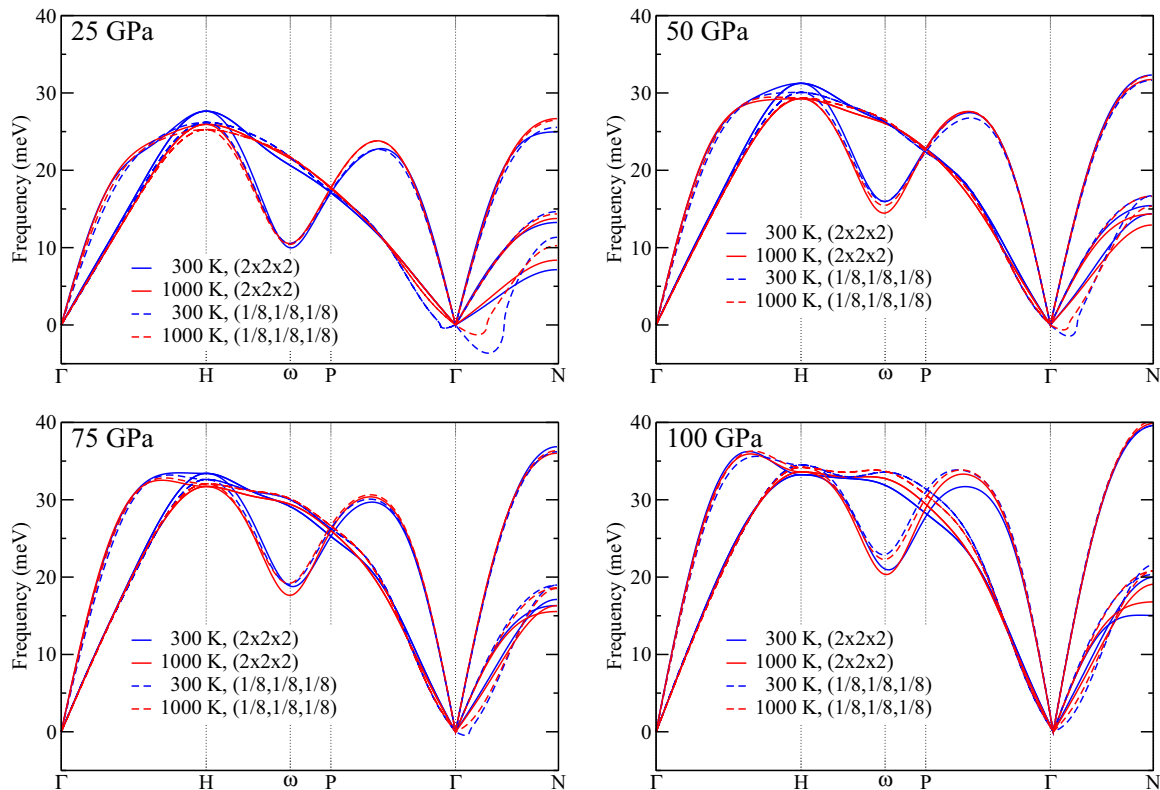


FIG. 8. Phonon spectra of bcc zirconium computed using A-TDEP for two temperatures 300 K (in blue) and 1000 K (in red) and around four pressures (25, 50, 75, and 100 GPa). The calculations using a  $(2 \times 2 \times 2)$  MP mesh are shown with solid lines and the calculations using a single  $(\frac{1}{8}, \frac{1}{8}, \frac{1}{8})$   $\mathbf{k}$  point are shown with dashed lines.

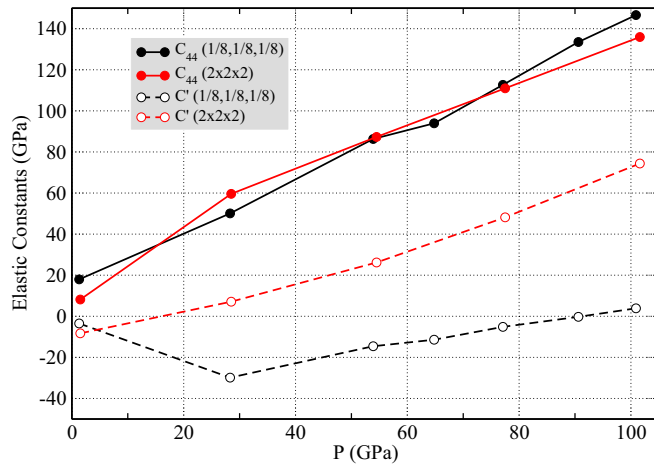


FIG. 9. Shear constants  $C_{44}$  and  $C'$  vs pressure at 300 K for two  $\mathbf{k}$ -point meshes: a  $(2 \times 2 \times 2)$  MP mesh and a single  $(\frac{1}{8}, \frac{1}{8}, \frac{1}{8})$   $\mathbf{k}$  point.

always stable when the  $2 \times 2 \times 2$  MP mesh is used ( $C' > 0$  when  $P > 20$  GPa).

## VI. CONCLUDING REMARKS

We have measured the 300 K compression curve of zirconium up to 142 GPa, in helium and neon pressure media. The measured sequence of phase transitions is  $\alpha$ -Zr  $\rightarrow$  ( $17 \pm 3$  GPa)  $\omega$ -Zr  $\rightarrow$  (35 GPa)  $\beta$ -Zr, which is stable up to 142 GPa. These transformations exhibit interesting microstructural features. The compression behaviors of the  $\alpha$ ,  $\omega$ , and  $\beta$  phases of Zr are similar to the homonym phases of Ti.

We suggest that nonhydrostatic compression effects (pressure gradients and/or lattice strains) explain the observation of an isostructural transition to  $\beta'$ -Zr with a 4% volume collapse in Ref. [13] at 58 GPa.

We have tried to reproduce the *ab initio* molecular dynamics calculations of Ref. [13], which also evidenced the formation of  $\beta'$ -Zr after one heating-cooling cycle above 55 GPa. After this cycle, the modeled system returns back to  $\beta$ -Zr in our runs. Using temperature-dependent effective potential formalism, we have determined the dynamical stability of  $\beta$ -Zr under different approximations within DFT. Computed phonon spectra clearly show that with the single  $\mathbf{k}$  point used in Ref. [13] runs,  $\beta$ -Zr is dynamically unstable up to 75 GPa at 300 K. With a  $(2 \times 2 \times 2)$  MP mesh,  $\beta$ -Zr is dynamically stable under pressure, in agreement with the experiments. The dynamical instability is hard to detect in standard molecular dynamics runs, but it may have frozen the system in an unstable state. To test this hypothesis, it would be interesting if Stavrou *et al.* were to perform new *ab initio* molecular dynamics simulations using a  $(2 \times 2 \times 2)$   $\mathbf{k}$ -point mesh.

## ACKNOWLEDGMENTS

We thank the European Synchrotron Radiation Facility and Diamond Light Source (In House Grant No. NT26782-4) for beamtime. We thank Florent Occelli for the help with sample loading and Volodymyr Svitlyk for helping during the experimental setup. S.A. acknowledges the support from the Natural Environment Research Council of Great Britain and Northern Ireland via Grants No. NE/M000117/1 and No. NE/M00046X/1.

- [1] E. Y. Tonkov and E. G. Ponyatovsky, *Phase Transformations of Elements Under High Pressure* (CRC Press, Boca Raton, FL, 2005).
- [2] S. K. Sikka, Y. K. Vohra, and R. Chidambaram, *Prog. Mat. Sci.* **27**, 245 (1982).
- [3] A. Dewaele, V. Stutzmann, J. Bouchet, F. Bottin, F. Occelli, and M. Mezouar, *Phys. Rev. B* **91**, 134108 (2015).
- [4] P. Parisiades, F. Cova, and G. Garbarino, *Phys. Rev. B* **100**, 054102 (2019).
- [5] D. Errandonea, Y. Meng, M. Somayazulu, and D. Hausermann, *Phys. B (Amsterdam, Neth.)* **355**, 116 (2005).
- [6] E. Cerreta, G. T. Gray III, R. S. Hixson, P. A. Rigg, and D. W. Brown, *Acta Mat.* **53**, 1751 (2005).
- [7] A. Dewaele, R. André, F. Occelli, O. Mathon, S. Pascarelli, T. Irifune, and P. Loubeyre, *High Press. Res.* **36**, 237 (2016).
- [8] D. Popov, N. Velisavljevic, W. Liu, R. Hrubciak, C. Park, and G. Shen, *Sci. Rep.* **9**, 15712 (2019).
- [9] O. Hellman, I. A. Abrikosov, and S. I. Simak, *Phys. Rev. B* **84**, 180301(R) (2011).
- [10] V. Y. Trubitsin and E. B. Dolgusheva, *Phys. Rev. B* **77**, 172302 (2008).
- [11] H. Xia, S. J. Duclos, A. L. Ruoff, and Y. K. Vohra, *Phys. Rev. Lett.* **64**, 204 (1990).
- [12] Y. Akahama, M. Kobayashi, and H. Kawamura, *J. Phys. Soc. Jpn.* **60**, 3211 (1991).
- [13] E. Stavrou, L. H. Yang, P. Söderlind, D. Aberg, H. B. Radousky, M. R. Armstrong, J. L. Belof, M. Kunz, E. Greenberg, V. B. Prakapenka, and D. A. Young, *Phys. Rev. B* **98**, 220101(R) (2018).
- [14] B. Amadon, S. Biermann, A. Georges, and F. Aryasetiawan, *Phys. Rev. Lett.* **96**, 066402 (2006).
- [15] J. S. Pigott, N. Velisavljevic, E. K. Moss, D. Popov, C. Park, J. A. Van Orman, N. Draganic, Y. K. Vohra, and B. T. Sturtevant, *J. Phys.: Condens. Matter* **32**, 12LT02 (2020).
- [16] M. Mezouar, W. Crichton, S. Bauchau, F. Thurel, H. Witsch, F. Torrecillas, G. Blattmann, P. Marion, Y. Dabin, J. Chavanne *et al.*, *J. Synchrotron Rad.* **12**, 659 (2005).
- [17] S. Anzellini, A. K. Kleppe, D. Daisenberger, M. T. Wharmby, R. Giampaoli, S. Boccato, M. A. Baron, F. Miozzi, D. S. Keeble, A. Ross *et al.*, *J. Synchrotron Rad.* **25**, 1860 (2018).
- [18] C. Prescher and V. B. Prakapenka, *High Press. Res.* **35**, 223 (2015).
- [19] A. Coelho, *J. Appl. Cryst.* **51**, 210 (2018).
- [20] A. Dewaele, M. Torrent, P. Loubeyre, and M. Mezouar, *Phys. Rev. B* **78**, 104102 (2008).
- [21] P. I. Dorogokupets and A. R. Oganov, *Phys. Rev. B* **75**, 024115 (2007).



- [22] X. Gonze, B. Amadon, G. Antonius, F. Arnardi, L. Baguet, J.-M. Beuken, J. Bieder, F. Bottin, J. Bouchet, E. Bousquet *et al.*, *Comput. Phys. Commun.* **248**, 107042 (2020).
- [23] P. E. Blöchl, *Phys. Rev. B* **50**, 17953 (1994).
- [24] M. Torrent, F. Jollet, F. Bottin, G. Zérah, and X. Gonze, *Comput. Mater. Sci.* **42**, 337 (2008).
- [25] N. Holzwarth, A. Tackett, and G. Matthews, *Comput. Phys. Commun.* **135**, 329 (2001).
- [26] F. Jollet, M. Torrent, and N. Holzwarth, *Comput. Phys. Commun.* **185**, 1246 (2014).
- [27] J. P. Perdew, K. Burke, and M. Ernzerhof, *Phys. Rev. Lett.* **77**, 3865 (1996).
- [28] B.-T. Wang, P. Zhang, H.-Y. Liu, W.-D. Li, and P. Zhang, *J. Appl. Phys.* **109**, 063514 (2011).
- [29] H. J. Monkhorst and J. D. Pack, *Phys. Rev. B* **13**, 5188 (1976).
- [30] F. Bottin, S. Leroux, A. Knyazev, and G. Zérah, *Comput. Mater. Sci.* **42**, 329 (2008).
- [31] K. Takemura, *J. Appl. Phys.* **89**, 662 (2001).
- [32] A. Dewaele and P. Loubeyre, *High Press. Res.* **27**, 419 (2007).
- [33] S. Zhang, X. Zhang, Y. Zhu, S. Zhang, L. Qi, and R. Liu, *Comput. Mater. Sci.* **61**, 42 (2012).
- [34] S. Anzellini, A. Dewaele, F. Occelli, P. Loubeyre, and M. Mezouar, *J. Appl. Phys.* **115**, 043511 (2014).
- [35] P. Vinet, J. H. Rose, J. Ferrante, and J. R. Smith, *J. Phys. Condens. Matter* **1**, 1941 (1989).
- [36] C. Meade and R. Jeanloz, *J. Geophys. Res.* **93**, 3261 (1988).
- [37] R. M. Vignes, R. Becker, J. Stoelken, and M. Kumar, *J. Appl. Phys.* **113**, 213503 (2013).
- [38] K. Takemura, *J. Phys. Soc. Jpn.* **76**, 202 (2007).
- [39] J. Zhang, Y. Zhao, P. A. Rigg, R. S. Hixson, and G. T. Gray, III, *J. Phys. Chem. Solids* **68**, 2297 (2007).
- [40] N. Velisavljevic, G. N. Chesnut, L. L. Stevens, and D. M. Dattelbaum, *J. Phys. Condens. Matter* **23**, 125402 (2011).
- [41] A. Dewaele, P. Loubeyre, F. Occelli, O. Marie, and M. Mezouar, *Nat. Commun.* **9**, 2913 (2018).
- [42] O. Hellman, P. Steneteg, I. A. Abrikosov, and S. I. Simak, *Phys. Rev. B* **87**, 104111 (2013).
- [43] O. Hellman and I. A. Abrikosov, *Phys. Rev. B* **88**, 144301 (2013).
- [44] F. Bottin, J. Bieder, and J. Bouchet, *Comput. Phys. Commun.* **254**, 107301 (2020).
- [45] J. Bouchet and F. Bottin, *Phys. Rev. B* **92**, 174108 (2015).
- [46] J. Bouchet, F. Bottin, V. Recoules, F. Remus, G. Morard, R. M. Bolis, and A. Benuzzi-Mounaix, *Phys. Rev. B* **99**, 094113 (2019).
- [47] J. Bouchet and F. Bottin, *Phys. Rev. B* **95**, 054113 (2017).
- [48] B. Dorado, F. Bottin, and J. Bouchet, *Phys. Rev. B* **95**, 104303 (2017).
- [49] X. Qian and R. Yang, *Phys. Rev. B* **98**, 224108 (2018).
- [50] A. Heiming, W. Petry, J. Trampenau, M. Alba, C. Herzig, H. R. Schober, and G. Vogl, *Phys. Rev. B* **43**, 10948 (1991).